Fabrication of porous Ni-Ti shape memory alloy via binder jet additive manufacturing and solid-state sintering

Iman Dashtgerd [a], Ashley Cahoon [b], Novin Rasooli [c], Milad Hemmati [d], Meisam Khademitab [a], Sayed M. Saghaian [a], Sayed E. Saghaian [d], Marcella Vaicik [b], Matthew Daly [c], Amir Mostafaei [a,] *

[a] Department of Mechanical, Materials and Aerospace Engineering, Illinois Institute of Technology, 10 W 32nd Street, Chicago, IL 60616, USA

[b] Department of Biomedical Engineering, Illinois Institute of Technology, 3255 South Dearborn Street, Chicago, IL 60616 USA

[c] Department of Civil, Materials, and Environmental Engineering, University of Illinois Chicago, 842 W. Taylor St, 2095 ERF (MC 246), Chicago, IL 60607 USA

[d] Department of Mechanical and Civil Engineering, Florida Institute of Technology, 150 W. University Blvd. Melbourne, FL, USA

* Corresponding author: mostafaei@iit.edu (A. Mostafaei)

Abstract

This paper explores the additive manufacturing of nickel-titanium (Ni-Ti) shape memory alloy (SMAs) using binder jetting and subsequent solid-state sintering under an Ar atmosphere. The consolidated 3D-printed Ni-Ti parts exhibit a correlation between pore morphology, pore fraction, and phase formation at different solid-state sintering temperatures. At a sintering temperature of 1175 °C, NiTi grains with TiC precipitates along grain boundaries are observed, accompanied by irregular, interconnected pores constituting ~15% of the volume. Increasing the sintering temperature to 1185 °C leads to the formation of a minor phase of Ni_4Ti_3 within NiTi grains, along with grain boundary TiC precipitates, and isolated pores with a volume fraction of ~5%. The higher sintering temperature corresponds to a higher average nanohardness value (8.1 GPa or 763 Hv compared to 6.9 GPa or 654 Hv), indicating the presence of a greater abundance of secondary phases and higher densification at the elevated sintering temperature. While the transformation temperatures (TTs) were undetectable in the bulk-printed samples, a different structure featuring designed channels and thin struts, sintered under similar conditions, exhibited detectable TTs, with a martensite start temperature of 34°C. Biocompatibility tests demonstrated cell spreading and attachment on both sintered Ni-Ti samples. These findings offer valuable insights into the potential use of binder jetted Ni-Ti for medical implants and tissue engineering applications.

Keywords: Binder jetting; Shape memory alloys; Microstructure analysis; Nanoindentation; Biocompatibility.

1. Introduction

In the past decades, research and development around Ni-Ti shape memory alloys (SMA), specifically in the medical industry, has been growing due to the enhancement of manufacturing technology and the needs of the market [1]. This material is suitable for load-bearing bone/tissue implants due to its light weight, corrosion resistance, biocompatibility, shape memory effect, and superplastic behavior [2,3]. Its austenite transformation temperatures typically range between 0 °C and 100 °C, with a temperature hysteresis of 25–40 °C [4]. The $Ni_{50.8}$-Ti composition is commonly used in pseudoelastic SMA components due to presenting superelastic behavior at room and body temperatures [5]. The transformation temperatures can be significantly altered by small changes in the Ni or Ti content. Ni-rich NiTi alloys undergo thermomechanical treatment involving the precipitation of metastable Ni_4Ti_3 and Ni_3Ti_2 phases, which affect martensite transformation temperatures and parent phase strengthening [6,7]. The concentration of point defects in shape memory intermetallics, influenced by composition or heat treatment, also impacts transformation temperatures (martensitic start and finish, M_s and M_f, respectively) and hysteresis [4]. Factors such as lattice defects, internal stress/strain fields, and precipitates can affect the mobility of martensite interfaces and consequently, the shape memory properties of the alloy.

Porous Ni-Ti has recently received much attention in biomedical applications [2,3,8–10]. Powder metallurgy is a common method of manufacturing Ni-Ti parts. It allows for the production of porous structures suitable for biomedical applications. Adjustment of mechanical properties by controlling impurity content and pore fraction is achievable [11–15]. Porous Ni-Ti allows direct nutrient transport, body fluid flow, and human tissue development [9]. The interaction between implanted devices and body tissues is usually influenced by the chemical and morphological characteristics of the pore wall surface. As the porous implant resides within the body, its pore space is filled with living tissues and fluids; thus, the pore size, distribution, and surface morphology significantly impact the integration of cell cultures within the pore surface of implant material. Consequently, materials featuring microporous structures in their pore walls are favored for cellular culture attachment. Ismail et al. [16] studied the effect of pore size (100-600 μm) and fraction (30-80%) on stiffness and comparable results close to human bone with desirable biocompatibility were observed. The Young's modulus of dense NiTi ranges from ~25-60 GPa. An engineered porous structure reduces the modulus to ≤ 20 GPa, closely mimicking human bone behavior and enhancing implant compatibility [16,17]. Several procedures have been previously

used to fabricate condensed Ni-Ti shape memory alloys, such as hot isostatic pressing [18], powder pre-alloying [19], elemental powder metallurgy [20], self-propagating hot synthesis [21], and thermohydrogen processing [22]. However, the production of complex geometries remains a main challenge in those methods that can be addressed by the emergence of additive manufacturing (AM) techniques.

Although laser powder bed fusion (L-PBF) has been widely used in AM for NiTi biomedical implants, it poses significant challenges, particularly with NiTi alloys. These challenges stem from high residual stresses caused by rapid cooling rates during the process, which can result in warping or cracking of the implant with complex shape. Moreover, the high operating temperatures during laser processing can induce alterations in the chemistry, solidified microstructure, and mechanical properties of NiTi-based alloys, potentially affecting their shape memory and superelastic characteristics [23–25]. Controlling the atmosphere during L-PBF is also problematic, leading to the potential introduction of impurities that may impact the biocompatibility and mechanical integrity of the implants [26,27].

In response to these challenges, binder jetting has emerged as a promising alternative to L-PBF [28,29] One of its key advantages is the avoidance of direct exposure to high temperatures, thereby reducing the risk of undesirable microstructural changes. Unlike L-PBF, binder jetting does not involve melting, resulting in part production without residual stresses and minimizing the likelihood of warping or cracking. Additionally, binder jetting allows production of biomedical implants at a lower cost with customizable porosity, which can be tailored for optimal bone ingrowth, enhancing stability and longevity. This method also offers greater control over material composition, which is crucial for minimizing impurities and ensuring the biocompatibility of NiTi implants. Although binder jet additive manufacturing is a multi-step process that includes both printing and post-process heat treatments like sintering, it offers significant advantages for producing porous biomaterials. Specifically, this technique allows for the introduction of a controlled pore fraction throughout the designed structure, making it highly beneficial for applications requiring tailored porosity [30–35].

This study aims to introduce the binder jetting technique to the production of porous NiTi alloys. Solid-state sintering is conducted to control pore fraction, phase formation, and to test structure-property relationships [36]. Additionally, the formation of grain boundary TiC in binder jetted Ni-Ti powder appears to be beneficial in enhancing strength and inhibiting the formation of

the undesired rhombohedral phase (R phase). This inhibition is due to the mismatch of thermal stresses between the Ni-Ti matrix and TiC [37]. This study also evaluates the cell viability and attachment of fibroblasts to determine Ni-Ti biocompatibility. Fibroblasts are the main connective tissue cells that support normal wound healing [38,39]. It is important for cell survival and for cells to adhere to the surface of a Ni-Ti implant as one aspect of successful osseointegration. To determine that nickel-titanium is a suitable material for long-term biomedical applications, we have evaluated the biocompatibility of the material.

2. Experimental Procedure

Powder – $Ni_{50.8}Ti_{49.2}$ powder (Ni-rich SMAs) was prepared by the electrode induction melting gas atomization (EIGA) technique with particle size distribution (PSD) of 15-53 µm and spherical morphology shown in Figure 1(A). The analyzed PSD showed D_{10} = 19.6 µm, D_{50} = 33.8 µm, and D_{90} = 50.7 µm and results are presented in Figure 1(B). The PSD falls within the typical range used for powder bed AM systems.

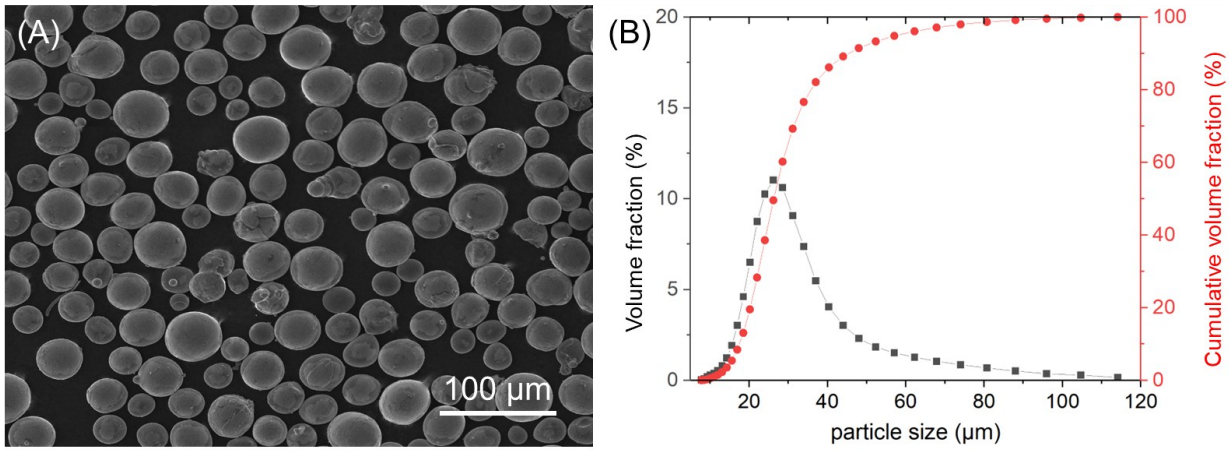

Figure 1. (A) Scanning electron microscopy image of NiTi powder using secondary electron imaging, and (B) particle size distribution analysis.

Sample Preparation – An ExOne Innovent^{+} binder jet printer was used to manufacture parts made of NiTi powder. An AquaFuse water-based binder (BA-005 solution) from ExOne Company was utilized, consisting of 10 vol% ethylene glycol monobutyl ether and 20 vol% ethylene glycol. Rectangular coupons, also named as bulk-printed samples, with dimensions of 7 mm × 5 mm × 6 mm were printed. By introducing engineered channels and thin struts samples, tiny struts with a cross-section area of 1 mm × 1 mm were also manufactured that are, at least, five times smaller

than the cross-section area of the bulk-printed sample (7 mm × 5 mm mm). To prevent possible oxidation of NiTi powder in air, curing was carried out in a vacuum oven at a temperature of 185±2 °C for 8 h. After depowdering, the parts were each encapsulated in quartz tubes under a vacuum of 10^{-6} bar. Capsules were purged and back-filled with argon gas five times to dilute oxygen concentration [40,41]. Encapsulated samples were placed in a box furnace and sintered at two temperatures of 1175 °C and 1185 °C under a hold time of 2 h. The selected temperatures were expected to result in different pore morphology and phase formation after sintering of binder jetted Ni-Ti powder. The selection of temperature and atmosphere was based on previous attempts to densify binder jetted NiTi alloys. Experimental findings showed that vacuum sintering was unsuitable for NiTi due to potential elemental evaporation and composition changes. A range of sintering temperatures (1100-1200 °C) were tested on binder jetted NiTi samples, and two temperatures that proved most effective for densification and microstructure evolution were selected for this study.

Characterization - X-ray diffraction analysis (XRD, Bragg-Brentano mode) was performed on samples (model Thermo ARL) with Cu-Kα radiation (λ = 1.54 Å, 35 kV and 30 mA) [42], with 2θ ranging between 30 and 90º, a scan speed of 1 s/step, and scan step of 0.02º at ambient temperature. The sintered coupons were sliced (using Mitsubishi FX10k Wire-EDM machine) parallel to the build direction along the XZ plane. Then, the sliced parts were hot-mounted using MetLab phenolic thermosetting molding powder. Subsequent steps involved grinding and polishing the mounted samples. The grinding process started with SiC sandpapers, progressively moving up to a P4000 grade for a smooth finish. Polishing was carried out using a 3 μm diamond abrasive, followed by 1 and 0.05 μm Al_2O_3 abrasives. The final polish was achieved using a 0.04 μm colloidal silica solution on a Buehler Phoenix 4000 platen grinder-polisher machine. To examine the pore morphology, size and distribution as well as grain structure, a Keyence VHX-7100 digital microscope was used. Also, the spatial distribution of pores was qualitatively and quantitatively analyzed using a ZEISS Metrotom 800 X-ray micro-computed tomography (μ-CT), operating at an energy of 130 kV and a current of 30 mA, and it was equipped with an Al 2.0 mm filter. The scanning parameters included averaging frames of 4 and an angular range of 360° with a step size of 0.12°. This setup achieved a spatial resolution of 5 μm/pixel, allowing for a detailed examination of the internal structure. The data was then reconstructed and analyzed using Volume Graphics Studio Max 3.5.1. A scanning electron microscope (SEM, JEOL 5900LV) equipped with

an Oxford Instruments energy dispersive spectroscopy (EDS) detector operating at an acceleration voltage of 20 kV and step size of 0.75 μm was used for microscopy and elemental mapping. In addition, the TA Instrument Differential Scanning Calorimetry 250 (DSC 250) with a heating/cooling rate of 10 °C/min in a nitrogen atmosphere was used to determine the transformation temperatures (TTs).

Vickers microhardness measurements were conducted (Buehler model Micromet 2) at a load of 100 gf and a dwell time of 10 s (twenty indentations). Nanoindentation experiments were conducted using a Femtotools NMT04 nanomechanical testing platform with a diamond Berkovich tip. The tip function and frame stiffness were calibrated using a fused silica reference, following standard procedures described by Oliver and Pharr [43]. For all indents, loading was executed at a rate of 1000 μN/s, with a 10 s hold at the peak load before initiating the unloading phase. During unloading, the load was removed at a rate of 500 μN/s. The sample was subsequently unloaded to 10% of the peak load and held at constant load for 100 s to collect data for thermal drift correction. An indentation array consisting of at least 20 indents was generated for the 1175 °C and 1185 °C sintered samples, with an indent spacing of 10 μm, and peak load ranging from 2000 μN to 5000 μN. The nanoindentation hardness is measured from the sample penetration depth at the peak load of the unloading segment and is natively calculated as a Meyer hardness (projected contact area definition) using the calibrated tip function. The nanohardness is also calculated on the Vickers scale (surface contact area definition) by assuming an idealized conversion between projected and surface contact areas.

Cell viability - An indirect assessment of biocompatibility of two binder jetted Ni-Ti samples with interconnected channels (400 μm) sintered at 1175 °C and 1185 °C was assessed through *in vitro* cytotoxicity assays conducted on mesenchymal mouse cells, 3T3 fibroblast cells (American Type Culture Collection (ATTC)), as previously described [35], in accordance with ISO 10993-5:2009(E) standards. 3D printed samples were then steam autoclaved to achieve sterilization. Samples were each submerged in a 50 ml conical tube of Dulbecco's Modified Eagle Medium (DMEM) + 10% fetal bovine serum (FBS) for 24 h at 37 °C to create NiTi-exposed leachates. On the same day, cells were seeded in a 48-well tissue culture-treated well plate at seeding density of 0.03×10^6 cells/well. Cells were incubated at 37 °C and 5% CO_2 with 0.4 ml of complete growth medium (DMEM, 10% FBS, 1% Penicillin-Streptomycin, and 1% L-Glutamine) for 24 h. After

24 h, cells were approximately 50-70% confluent and the complete growth medium was removed. Ni-Ti leachates were mixed with a vortex mixer immediately before they were used for cell culture. Media was replaced with 0.4 ml of DMEM + 10% FBS as the control group, Ni-Ti 1175 °C leachate as experimental group 1, and Ni-Ti 1185 °C leachate as experimental group 2. 3T3 fibroblasts were cultured with control and experimental medias for 1 day. After 1 day of culture with the leachates, cells were stained with Calcein AM and Ethidium Homodimer-1 in accordance with the manufacturer's protocol for the LIVE/DEAD Viability/Cytotoxicity Kit for Mammalian Cells by ThermoFisher Scientific [35]. Cells were imaged with a Nikon A1 HD25 confocal imaging system with fully motorized Nikon Eclipse Ti2-E inverted microscope with epifluorescence [35]. Images were analyzed in ImageJ to determine the percentage of viable cells by counting cells stained green (live) and cells stained red (dead) within each well. This procedure was then repeated for a long-term experiment of 3T3 fibroblasts cultured in the Ni-Ti leachates for 5 days. Cells were incubated at 37 °C and 5% CO_2 for 5 days with regular media changes every 2-3 days, in accordance with the International Organization for Standardization (ISO) ISO 10993-5:2009(E) standards [44]. Figure 2 demonstrates the experimental setup for cell viability.

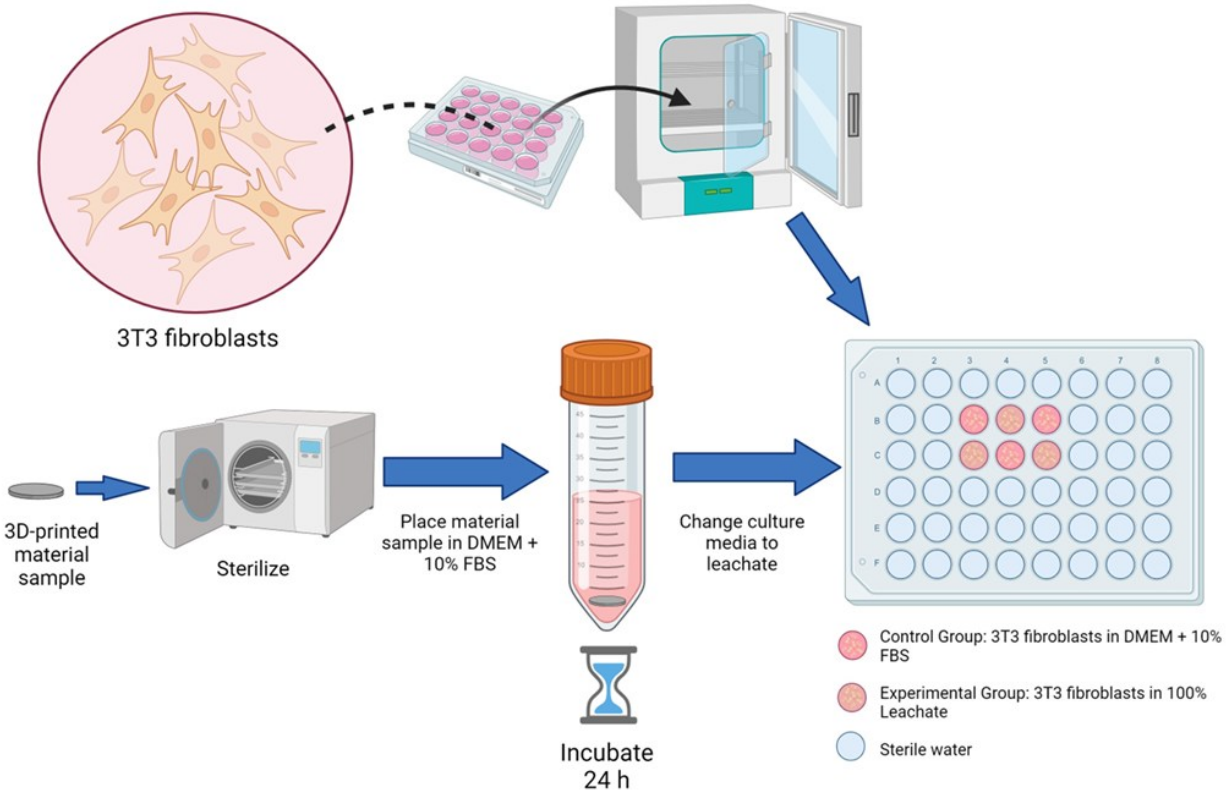

Figure 2. Experimental setup for preparing and culturing 3T3 fibroblasts with Ni-Ti leachates.

Cell attachment - A direct assessment of 3T3 fibroblast cell contact and attachment with both Ni-Ti samples was conducted, in accordance with ISO 10993-5:2009(E) standards. Ni-Ti samples were autoclaved to achieve sterilization. 3T3 fibroblast cells were cultured in a T-75 flask until they reached 80% confluency, observed through inverted microscopy. Media was removed from the flask and cells were briefly rinsed with 5 ml of Phosphate Buffered Saline (PBS). PBS was aspirated and 5 mL of Trypsin-EDTA was added to the flask. The flask was incubated at 37 °C and 5% CO_2 for 4-6 minutes to allow cells to detach from the bottom of the flask. Cells were observed with the inverted microscope to ensure the cells had detached and dispersed from the bottom of the flask. A complete growth medium (5 ml) was added to the flask and this mixture of media and cells was pipetted into a 15 ml conical tube. Cells were spun down in a centrifuge at 200 g-force for 5 min at room temperature. Media was aspirated leaving only a couple of microliters so that the cell pellet was not disturbed. Cells were resuspended in 3 ml of complete growth medium and were homogenized via slow and gentle pipetting. To determine the cell count, 50 µl of cell suspension was transferred into a 1.5 ml microcentrifuge tube and mixed with 50 µl of Trypan Blue Solution. Cells stained with 10 µl of Trypan Blue were transferred into the counting chamber of a hemocytometer covered with a glass coverslip. The inverted microscope was used to observe the hemocytometer to count the number of cells in four squares. Cells that were stained blue were recorded as dead and cells that were not stained were counted as alive. The total cell count was calculated from the average number of cells per square, the cell resuspension volume, the Trypan Blue dilution factor, and the hemocytometer factor. Next, the 3T3 fibroblast cells were stained following the manufacturer's instructions for PKH26 Red Fluorescent Cell Linker Mini Kit for General Cell Membrane Labeling (Sigma-Aldrich), as previously described [35]. After the cells were stained, 5.775×10^4 cells/sample suspended in 10 µl of the cell solution was pipetted onto the surface of the 3D printed Ni-Ti samples that were placed in a 24-well tissue culture treated well plate. The samples were incubated for 45-60 minutes and then 1 ml of DMEM + 10% FBS was added to the wells with the samples. The samples were then incubated for 24 h to allow for adequate cell attachment. After 24 h the samples were flipped over and transferred into a new 24-well plate for imaging. Cells were imaged with a Nikon Eclipse Ti2 confocal microscope. Samples were flipped over to image the bottom of the sample in addition to the top. Both samples had interconnected channels which are large openings that cells could have traveled through. Cells were only directly seeded on the top surface of the samples; however, it is important to see if cells

traveled through the interconnected channels to the bottom surface of the samples. The obtained images were analyzed with ImageJ to obtain the average area of cell attached to the sample. Cells were formalin fixed to both Ni-Ti samples for characterization by scanning electron microscopy. Briefly, in a 24-well plate Ni-Ti samples were rinsed with 100 µl of PBS. PBS was removed and 100 µl of 10% formalin was pipetted onto the Ni-Ti samples and the well plate was covered and incubated at room temperature for 15 min. Formalin was removed and the samples were rinsed with 100 µl of PBS three more times. Ni-Ti samples were moved into a dry 24-well plate and allowed to air dry for 48 h. Samples were loaded into the SEM chamber and were imaged with an acceleration voltage of 5 kV using secondary electron imaging.

3. Results and Discussion

3.1. Density and pore analyses

The densification behavior, pore morphology and its size distribution in the sintered NiTi samples manufactured through binder jetting were examined using optical microscopy and micro-computed tomography, and the findings are shown in Figure 3. The optical micrographs revealed irregular, interconnected pores in the sample sintered at 1175 °C, whereas the sample sintered at 1185 °C exhibited isolated pores with a mixed irregular/spherical pore morphology. Quantitative pore analysis using µ-CT indicated a pore size distribution ranging from 200 µm to 1.6 mm in the sample sintered at 1175 °C, whereas a slight increase in temperature to 1185 °C resulted in pore sizes ranging from 10 to 200 µm. Additionally, the horizontal interconnected pores formed during the binder jetting process, which were visible in the sample sintered at the lower temperature. This phenomenon is known to be related to the binder-powder interaction and the formation of ballistic defects in each discrete layer [45–47]. At higher temperatures, diffusion-driven particle rearrangement and densification played a key role in mitigating this in-process defect. As the temperature increased, atomic diffusion became more active, promoting enhanced mass transport across particle boundaries [46,48,49]. This accelerated diffusion facilitated the movement and redistribution of atoms, allowing particles to better rearrange, fill voids, and reduce pore sizes. As a result, the enhanced diffusion mechanisms at elevated temperatures led to improved bonding between particles, contributing to the elimination of defects that were present at lower sintering temperatures, and thus increasing the overall density and uniformity of the microstructure. Pore

analysis conducted on both optical and tomography micrographs indicated the presence of 15.4 vol.% of pores in the sample sintered at 1175 °C, whereas the pore fraction decreased to 5.1 vol% in the sample sintered at 1185 °C. Optical images showed area fractions of pores, which matched the volume fraction measured by μ-CT. Pores can act as stress concentrators, reducing the load-bearing cross-sectional area, which may lead to decreased mechanical strength, lower fatigue resistance, and reduced ductility [42]. Higher porosity can contribute to premature failure under tensile or cyclic loading due to crack initiation and propagation from pore sites. Therefore, minimizing porosity through optimized sintering conditions is critical for improving the mechanical performance of binder jetted materials, as densification directly correlates with enhanced strength and durability.

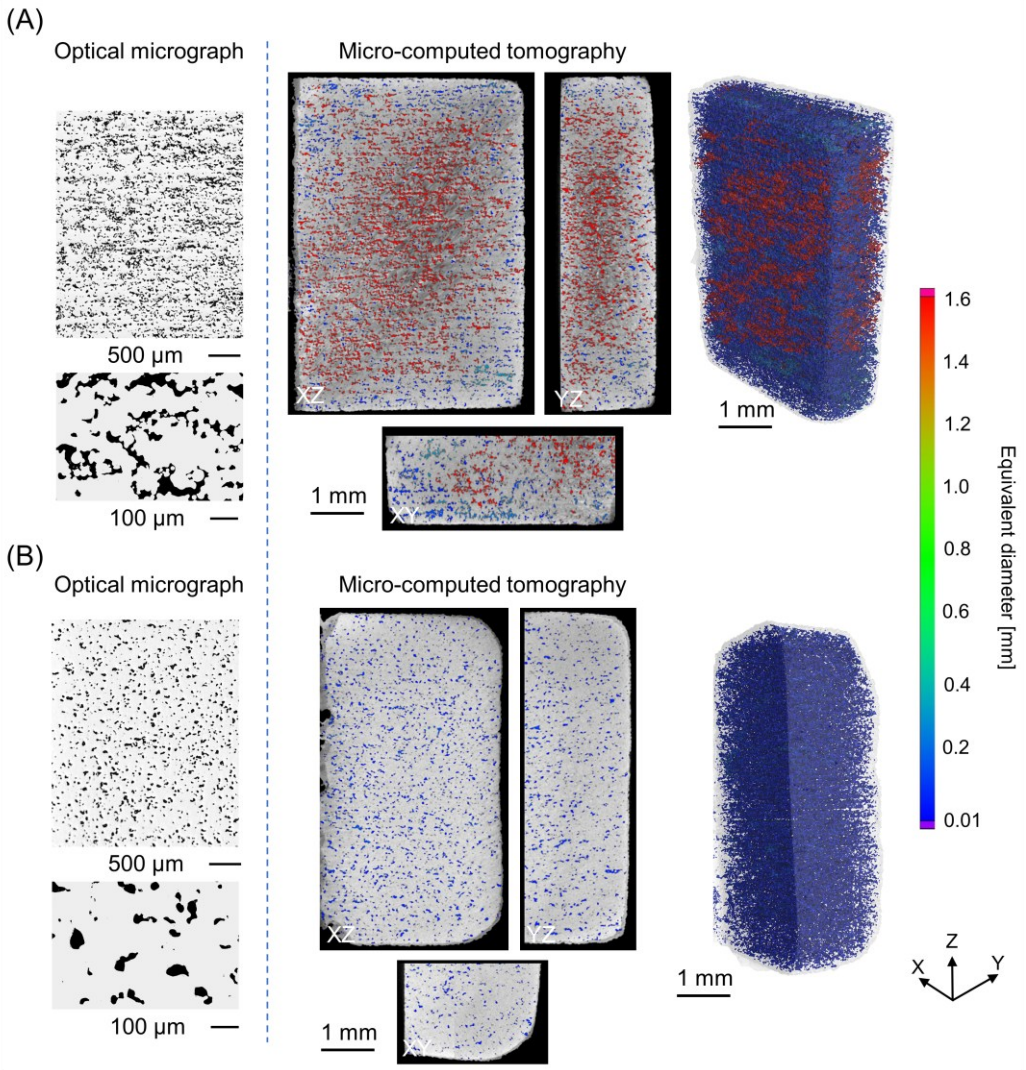

Figure 3. Analysis of densification, pore morphology and size distribution of binder jetted NiTi parts (A) sintered at 1175 °C and (B) sintered at 1185 °C.

3.2. Microstructure and phase analyses

To assess microstructure evolution during sintering, SEM micrographs and elemental analysis using EDS were collected. Figure 4 (A,B) displays high-magnification SEM micrographs taken from the polished surfaces alongside EDS elemental analysis, featuring both mapping and point analyses. According to the EDS findings, the sample sintered at 1175 °C exhibited a distribution of Ti- and C-rich regions at the grain boundaries (points 1-3), forming TiC with size ranging from 500 nm to 4 µm. The grains are comprised of Ni and Ti, indicating the presence of the NiTi phase (points 5-7). Additionally, trace amounts of NiTi-C were detected at the grain boundaries (point 4). Ni_4Ti_3 is a metastable phase commonly generated during the heat treatment of NiTi alloys, where it precipitates and contributes to material strengthening [50–52]. Sintering at 1185 °C also revealed a distribution of Ti- and C-rich regions at the grain boundaries (points 1,2) forming TiC with grain size ranging from 500 nm to 4 µm. The dominant phase was comprised Ni and Ti, indicating the presence of the NiTi compound (points 6,7). In addition, Ni-rich areas with lower Ti concentration were also detected, indicative of Ni_3Ti phase formation. Formation of Ni_3Ti phase at higher sintering temperature was related to Ti depletion in NiTi regions due to TiC formation at the grain boundaries, thus, Ni_3Ti phase formed in the microstructure which was detected at bright regions (points 3-5). The presence of both TiC and Ni_3Ti can negatively affect the shape memory properties of NiTi alloys by altering the phase transformation behavior. Ni_3Ti, being a brittle intermetallic phase, can reduce the material's ability to undergo the reversible martensitic transformation essential for shape memory effects. Additionally, TiC precipitates at grain boundaries can act as obstacles to transformation, further degrading the alloy's shape memory and superelastic properties. Since a Ti sponge was used as an oxygen getter during sintering experiments, no oxide compound was detected on the SEM-EDS micrographs.

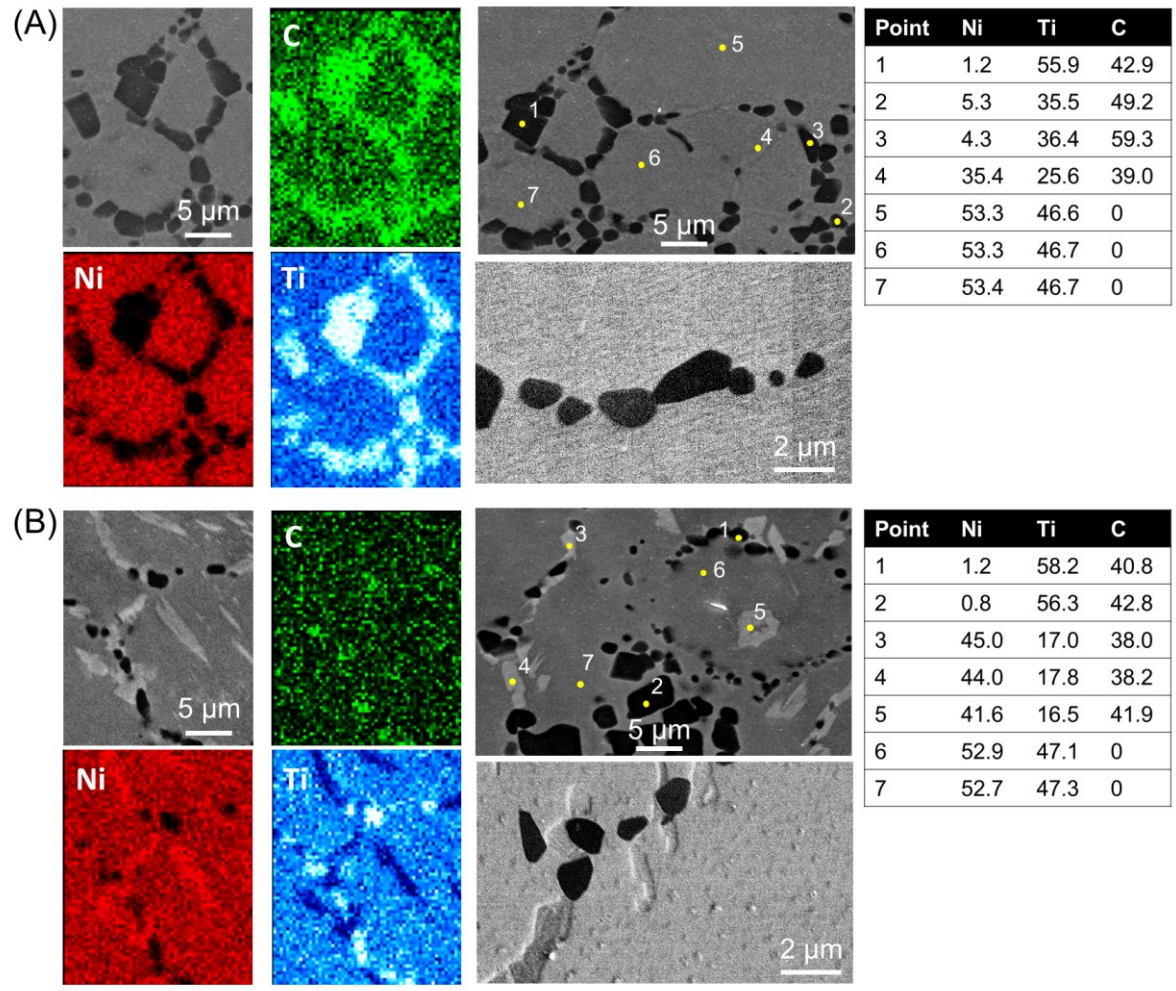

Point	Ni	Ti	C
1	1.2	55.9	42.9
2	5.3	35.5	49.2
3	4.3	36.4	59.3
4	35.4	25.6	39.0
5	53.3	46.6	0
6	53.3	46.7	0
7	53.4	46.7	0

Point	Ni	Ti	C
1	1.2	58.2	40.8
2	0.8	56.3	42.8
3	45.0	17.0	38.0
4	44.0	17.8	38.2
5	41.6	16.5	41.9
6	52.9	47.1	0
7	52.7	47.3	0

Figure 4. Scanning electron micrographs (secondary electron) and elemental analysis (map and point EDS results in at.%) revealing the microstructure and distribution of elements in different phases in NiTi samples sintered at two different temperatures of (A) 1175 °C and (B) 1185 °C.

The XRD patterns of the Ni-Ti samples sintered at 1175 °C and 1185 °C are shown in Figure 5, indicating the presence of NiTi, Ni_3Ti, Ni_4Ti_3, and TiC phases. Additionally, the sample sintered at 1185 °C showed possible formation of the $NiTi_2$ phase. The formation of the $NiTi_2$ phase at the higher sintering temperature is attributed to its thermodynamic favorability compared to the NiTi phase [51,53].

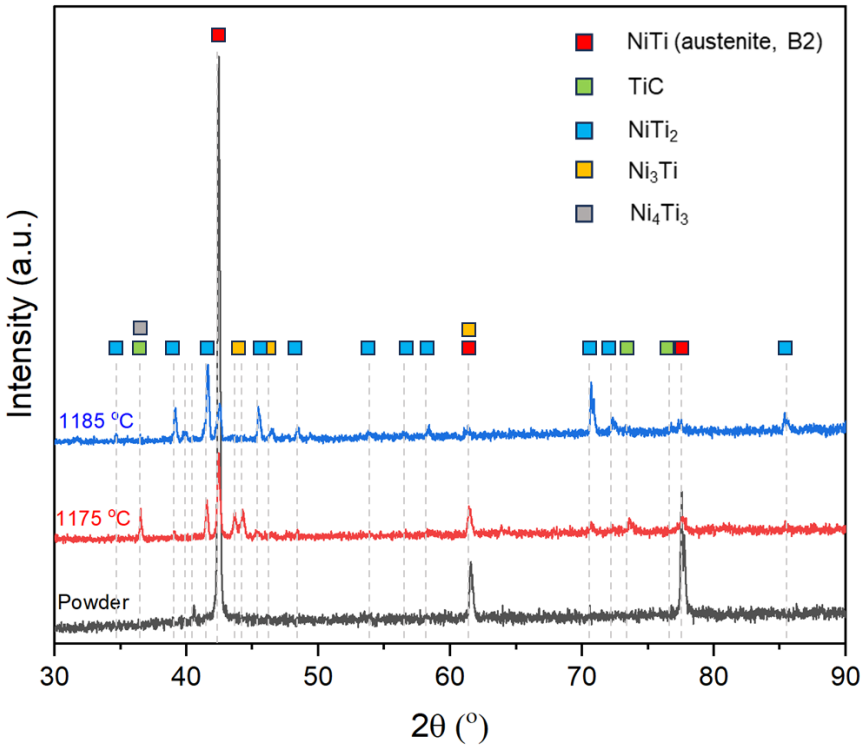

Figure 5. X-ray diffraction patterns of the NiTi powder and binder jetted parts sintered at two different temperatures. The background baselines have been shifted to the y-axis to allow for easy comparison.

3.3. Transformation temperatures

The Differential Scanning Calorimetry (DSC) results in Figure 6 showed the transformation temperatures (TTs) of powder and two different sintering conditions at 1175 °C and 1185 °C for the bulk-printed part and the structure with designed channels and thin struts. The austenite start and finish temperatures (A_s and A_f) during heating and martensite start and finish temperatures (M_s and M_f) during cooling were calculated using the tangent line method. For the powder, the TTs were A_s = -25.5 °C, A_f = 30.5 °C, and M_s = 6 °C. The M_f was below -60 °C and could not be captured due to experimental limitations. After binder jet printing followed by sintering, no peaks could be detected for dense specimens, while they appeared for the structure with designed channels and thin struts with TTs of A_s = -1 °C, A_f = 70 °C, M_s = 34 °C, and M_f = -36.5 °C. Since similar printing and post-processing conditions were applied for the bulk-printed part and the structure with designed channels and thin struts, the reason for this different behavior can be rooted in the design factors. By introducing engineered channels and thin struts samples, tiny struts with

a cross-section area of 1 mm × 1 mm were created that are, at least, five times smaller than the cross-section area of the bulk-printed sample (7 mm × 5 mm mm). Decreasing the dimension of samples at the same sintering conditions (time and temperature) provides a higher ratio of thermal energy to the cross-section area of the sample during the sintering process and a higher cooling rate from sintering temperature to the room temperature. These various thermal boundary conditions potentially resulted in different microstructural evolution that resulted in different DSC results for the bulk-printed part and the structure with designed channels and thin struts. These results demonstrate the geometry dependency of the sample's microstructure and indicate the need for further studies to explore the relationship between geometry and sintering conditions. This behavior was also observed in L-PBF of metals [54].

Thus, a more homogeneous microstructure generated at the structure with designed channels and thin struts sample compared to the bulk-printed one leads to the observed solid-state phase transformation. However, the DSC peaks of the sintered structure with designed channels and thin struts were broad and shifted to higher temperatures compared with powder. The TTs increase was due to the formation of Ni-rich secondary phases that were depicted in SEM results (such as Ni_4Ti_3 and Ni_3Ti), which caused Ni depletion in the matrix, followed by an increase in TTs. In addition, microstructural areas with varying Ni content resulted in broader DSC peaks [55]. Thus, changes in composition are the main factor in shifting or broadening/removing the peaks [56]. The presence of secondary phases such as Ni_3Ti and TiC can cause additional heat absorption or release events during the heating/cooling cycle of DSC. These events may overlap with the main transformation peak of NiTi, making it challenging to distinguish and potentially leading to a broader or less defined peak. Furthermore, the presence of unsuitable secondary phases that are not coherent and/or evenly distributed in the microstructure of NiTi samples can hinder the reversibility of the martensitic transformation and prevent the movement of domain boundaries during the transformation process, resulting in incomplete or no phase transformations. It should be noted that further heat treatments, such as solution annealing combined with aging, can be employed to rearrange the microstructure of dense samples to potentially provide more suitable microstructural conditions to present solid-solid transformation and also to adjust the TTs for specific medical applications [5,56].

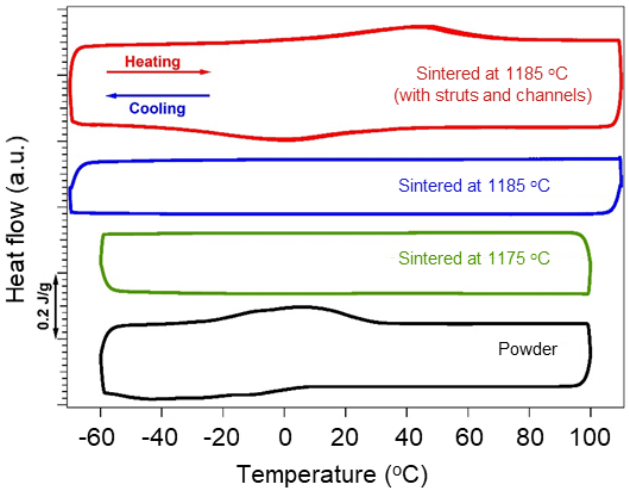

Figure 6. DSC curves of NiTi powder, bulk-printed samples or the structure with designed channels and thin struts sintered at 1175 °C and 1185 °C for representing reverse and forward transformations during heating and cooling cycles, respectively. The binder jetted sample with channels and struts was only sintered at 1185 °C.

3.4. Microstructure formation mechanism

Figure 7 presents a schematic illustration of the proposed microstructure evolution during the consolidation of binder jetted Ni-Ti powder through solid-state sintering. The consolidation process in sinter-based additive manufacturing includes three stages (1) initial stage sintering in which sinter necks form due to surface diffusion, (2) intermediate sintering stage in which density increases due to volumetric diffusion, leading to shrinkage and pore closure, and (3) final stage where grain coarsening may occur. Typically, when a binder jetted part with about 50% porosity is heated to about $0.95T_m$ (T_m is the solidus temperature of metallic materials), the driving force for sintering is the reduction of internal interfaces and surface energy. Mass transport, driven by the desire to reach a lower energy state, occurs between the particles. ***Stage 1***: Neck formation reduces total surface curvature, lowering system energy as material moves from convex surfaces (particles) to concave surfaces (necks), resulting in a 2-3% shrinkage and a relative density of about 65% is achieved. ***Stage 2***: Particle rearrangement occurs, forming interconnected irregular pores or isolated mixed irregular/spherical powders at grain boundaries, with substantial densification up to ~92%. ***Stage 3***: Densification continues at a slower rate, eliminating closed pores to achieve maximum density. During this stage, grain and pore coarsening may occur if maximum density over 99% is not achieved [57,58].

In this study, NiTi was additively manufactured using a binder jetting process, where a water-based binder selectively bound particles to form a 3D object. The binder jetted parts underwent a binder burnout step before sintering at the maximum temperature. The solidus temperature of the used Ni-Ti powder is approximately 1310 °C [59], although contamination from the binder (such as C) potentially lowers this temperature. Ti has a high tendency to react with C, forming TiC at the grain boundaries. The formation of TiC was similar at both applied temperatures, but pore evolution differed. The ratio of Ti to C (at. %) was 57:43 (i.e., EDS point analysis 1 in Figure 4), indicating TiC formation. Sintering at 1175 °C, consolidation with interconnected pores of irregular morphology and a final relative bulk density of 85% occurred. In contrast, sintering at 1185 °C resulted in isolated pores with a relative bulk density of 95%. The 1175 °C fell within the intermediate sintering regime, while the 1185 °C fell within the transition from intermediate to final stage sintering. The analyzed microstructures showed grain sizes similar to the starting powder size, indicating no grain coarsening, which was associated with the TiC formation and hindering grain growth. It is worth noting that powder and binder chemistry are important in binder jetting. For instance, Fe-based compounds are less likely sensitive to C contamination [42,48,60–62], however, Ni-Mn-based shape memory alloys [40,41,63], Cu alloys [64], and hard metals [65,66] showed sensitivity to C contamination. An alternative solution to minimize C contamination is using a clean burn-off binder which is a new area of research in metal binder jetting [67].

Ti atoms tended to migrate toward the grain boundaries to form TiC particles, leading to Ti-depleted regions around these particles. This had two effects including (1) supersaturation of Ni in these Ti-lean regions, increasing nucleation rates for Ni_4Ti_3 precipitates within and at the grain boundaries (i.e., EDS point analysis 4 in Figure 4) and (2) the formation of intermetallic precipitates such as Ni_4Ti_3 preferentially nucleating along crystallographic defects due to their higher surface energy. At the higher sintering temperature of 1185 °C, $NiTi_2$formed due to local chemistry heterogeneities. Additionally, Ni_3Ti was detected in this sample, associated with further migration of Ti from the matrix to the boundaries, leading to the formation of Ni-rich compounds such as Ni_3Ti. Finally, the matrix showed that the ratio of Ni to Ti (at. %) was 53 to 47, suggesting that NiTi was the dominant phase.

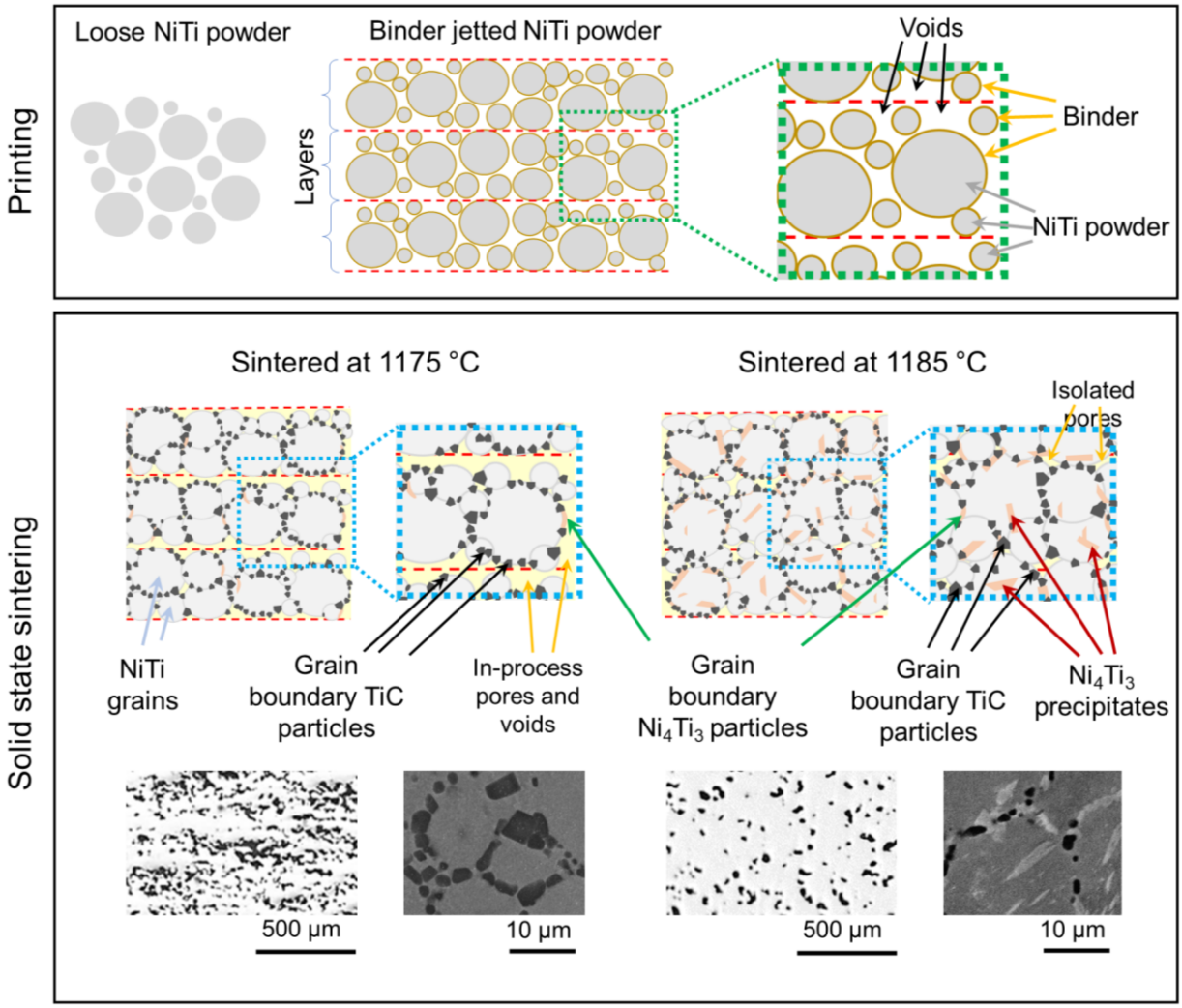

Figure 7. Schematic illustration of the proposed microstructure evolution during consolidation of binder jetted Ni-Ti powder through solid-state sintering. The layer thickness in printing step is defined as 100 µm. After the printing process, the surfaces of the powder particles are coated with binder. During the sintering cycle, a binder burnout step is conducted to remove the binder, followed by a temperature ramp-up to the sintering stage. The temperatures are kept below the solidus point of the NiTi alloy to promote shape retention while shrinkage and densification occur. The microstructure and phase evolution during the sintering stage are detailed in the study, see the solid-state sintering illustration.

3.5. Mechanical behavior

The results of nanoindentation experiments are provided in Figure 8, with nanohardness measurements expressed in both Meyer (GPa) and Vickers (HV) descriptions. The sample sintered at 1185 °C exhibited a higher nanohardness value, with an average of 8.1±2.1 GPa (763 HV), compared to the 1175 °C sample, which displayed a lower average nanohardness value of 6.9±1.2 GPa (654 HV). We attribute the disparities in the average nanohardnesses to differences in the

precipitate microstructure and the increased densification in the 1185 ºC sintered sample. This interpretation is supported by an examination of the scatter in nanohardness measurements, as shown in Figure 8(A). Here, the complete nanoindentation dataset is graphed as box and whisker plots showing the median (horizontal lines) and interquartile range (bar) of the nanohardness measurements. The whiskers span individual measurements falling within 150% of the interquartile range. At the largest indentation loads, the side length of the nanoindentation imprints is ~ 1 μm, which matches the size of key microstructural features. Therefore, large variations in nanohardness measurements are anticipated as the hardest (i.e., carbide precipitates) and softest (i.e., pores) features of the microstructure are selectively probed within nanoindentation volumes. Figure 8(B,C) provides the individual depth-resolved indentation curves for each sample. Here, the large scatter in nanohardness measurements is again evident, where some lower load indents penetrate further into the sample than experiments performed at higher indentation loads. Furthermore, the curvature of loading paths varies dramatically between individual indents, which is indicative of indentation upon microstructure phases with large differences in mechanical properties. We attribute the drift of indents during holding at peak loads with creep in the Ni-Ti microstructure, which is well known to occur in the indentation of NiTi SMAs with austenite transformation temperatures near room temperature [68]. Vickers microindentation experiments, which represent a bulk homogenization of microstructure features, yielded microhardnesses of 633±50 and 703±38 $HV_{0.1}$ for the 1175 and 1185 ºC sintered samples, respectively. These values fall within the statistical bounds of nanoindentation experiments, which further supports our interpretation of nanoindentation results. Several factors influence the microhardness of NiTi samples, including porosity, grain size, and the type and fraction of harder phases appeared in the microstructure, such as Ni_3Ti. At lower sintering temperatures (i.e., 1175 °C), the effect of porosity is predominant (pore fraction of ~15%), resulting in lower average nanohardness values, while sintering at higher temperature (i.e., 1185 °C) increased the nanohardness, which is attributed to a reduced amount of porosity (pore fraction of ~5%) and the inherent high hardness of the phases present in the microstructure. The matrix grain size is controlled by the grain boundary TiC (mainly) and Ni_3Ti phases. The Ni_3Ti phase, known for its superhard properties, contributes significantly to the increased hardness in the Ni-Ti system. Additionally, the NiTi-B2 phase also enhances hardness due to its higher strength compared to the NiTi phase. As a result, the combination of Ni_3Ti, NiTi-B2, and $NiTi_2$ phases in the sample sintered at 1185°C leads to an

overall increase in hardness. The hardness achieved in the binder jetted NiTi sample examined in this study surpasses that reported in other studies [69–72]. Given that one of the limitations of NiTi implant materials is their hardness and wear resistance, obtaining very high hardness values combined with the alloy's biocompatibility properties presents a significant potential for the manufacturing of Ni-Ti alloys using the binder jetting and solid-state sintering method. This combination could enhance the performance and durability of NiTi implants, making them more suitable for medical applications.

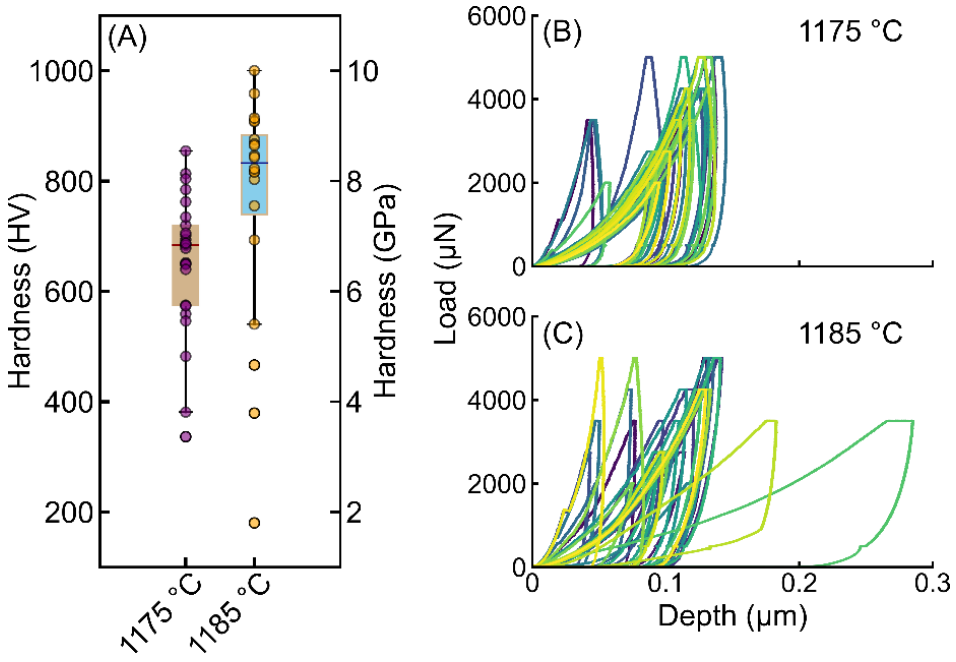

Figure 8. (A) Nanohardness measurements from Ni-Ti samples presented as Meyer (GPa) and Vickers (HV) hardnesses. This data is graphed as a box and whisker plot (see main text for the interpretation of plot features). The depth-resolved indentation curves collected from nanoindentation experiments are shown for samples sintered at 1175 °C (B) and 1185 °C (C).

3.6. Biocompatibility

Cell viability – The average percentage of live and dead cells on day 1 and day 5 (n = 6) is presented in Figure 9. Cells that stained green were live cells, and cells that stained red were dead cells. The average percentage of live/dead cells was recorded on day 1 (see Figure 9A) of cells exposed to DMEM + 10% FBS (control) and Ni-Ti leachates (experimental). The control group averaged 97.6 ± 2.8% live cells. This average percentage of live cells was consistent and expected for fibroblasts cultured with DMEM + 10% FBS. Cells exposed to Ni-Ti 1175 °C leachate

(experimental group 1) resulted in an average of 95.9 ± 3.1% live cells. Cells exposed to Ni-Ti 1185 °C leachate (experimental group 2) resulted in an average of 96.8 ± 2.2% live cells. From visual observation of the cell morphology, the 3T3 fibroblasts had less cell aggregation in the Ni-Ti leachates and the cells were better dispersed than the cells in the control medium. Despite this response, cells cultured with Ni-Ti leachates resulted in approximately 1% decreased cell viability compared to the control group.

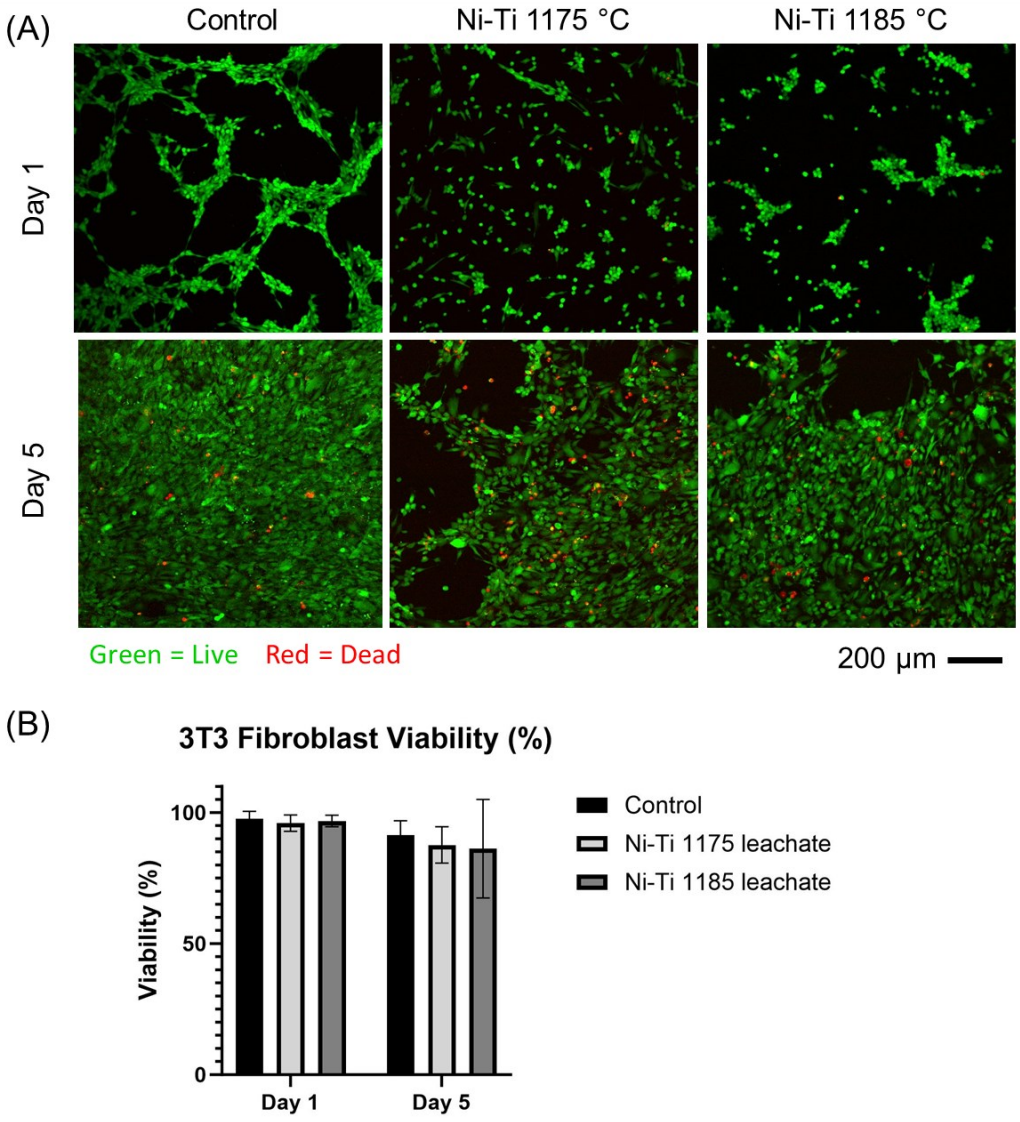

Figure 9. 3T3 fibroblast cell viability after exposure to Ni-Ti leachates for 1 and 5 days. (A) 3T3 fibroblast cells were cultured in DMEM + 10% FBS as the control group as well as the experimental group 1 including fibroblasts cultured in Ni-Ti 1175 °C leachate + DMEM + 10% FBS and the experimental group 2 including fibroblasts cultured in Ni-Ti 1185 °C leachate + DMEM + 10% FBS. Cells stained green are live cells and cells stained red are dead cells. For all groups (B) cell viability observed on day 1 was 95.9-97.6% live cells and cell viability at day 5 was 86.2-91.5% (n = 6).

The average percentage of live/dead cells was recorded on day 5 of cells exposed to growth media and Ni-Ti leachates (see Figure 9A). The control group averaged 91.5 ± 5.3% live cells. Cells exposed to Ni-Ti 1175 °C leachate (experimental group 1) resulted in an average of 87.6 ± 6.9% live cells. Cells exposed to Ni-Ti 1185 °C leachate (experimental group 2) resulted in an average of 86.2 ± 18.8% live cells. There is a greater variability of cell viability within this group, however the majority of cells in this group were recorded as live. For all groups (Figure 9B) the average cell viability was observed at day 1 of 95.9-97.6% live cells and cell viability at day 5 of 86.2-91.5%. After 5 days of exposure to Ni-Ti leachates, the percentage of live cells decreased in comparison to results from day 1. This decrease is statistically significant. Cell viability is expected to exhibit a minimal decrease in live cells compared to day 1 as there is more time for cell proliferation. Average cell viability on day 5 does not reduce by more than 30%, therefore this is not considered a cytotoxic effect, in accordance with ISO 10993-5:2009(E). These results support favorable survival and growth of 3T3 fibroblasts exposed to elemental Ni-Ti leachate.

Cell viability was assessed by conducting statistical analysis using two-way ANOVA. Days of culture had a statistically significant ($p < 0.05$) effect on cell viability results ($p = 0.0180$). Culture medium had no significance on cell viability results ($p = 0.5900$). The interaction of days and culture medium had no significance on cell viability results ($p = 0.8476$). See Table 1 for a summary of these results. Therefore, the longer number of days cells were cultured influenced cell viability. This is expected as cells proliferate and can occupy the entire area of the well and can exceed the capacity of the medium, which can limit and ultimately decrease further growth of the cells.

Table 1. Two-way ANOVA statistical analysis results of cell viability. P values were statistically significant when $p < 0.05$ and not significant when $p > 0.05$. Days of culture had a statistically significant effect on cell viability ($p = 0.0180$). Culture medium had no significance on cell viability ($p = 0.5900$). The interaction of days and culture medium had no significance on cell viability ($p = 0.8476$).

Source of Variation	**P value**	**Significance**
Days of Culture	$p = 0.0180$	Significant
Culture Medium	$p = 0.5900$	Not significant
The Interaction of Days and Culture Medium	$p = 0.8476$	Not significant

Cell attachment: After 24 h of contact with Ni-Ti samples, PKH26 stained 3T3 fibroblast cells successfully spread and adhered to both Ni-Ti surfaces, shown in Figure 10. Both Ni-Ti samples had designed channels and residual pores after sintering (interconnected ones in 1175 °C sample and isolated ones in 1185 °C sample) to which the cells were able to spread and adhere. As seen in Figure 10(A,C), cells attached on the top surface of the samples where the droplet was placed, attached inside the channel walls and to the bottom of the surface seen in Figure 10(B,D). From these images cells were counted and the percentage area occupied by the cells was determined. The average percentage area of cells attached to the top surface of Ni-Ti 1175°C sample (Figure 10A) was 11.6 ± 8.0% and for the bottom surface (Figure 10B) 2.0 ± 1.0%. The average percentage area of cells attached to the top surface of Ni-Ti 1185°C sample (Figure 10C) was 3.5 ± 3.0% and for the bottom surface (Figure 10D) 1.1 ± 1.0%. The cell droplet is placed on the top surface of the samples; therefore, it is reasonable that there was a larger percentage of cell attachment to the top surfaces of both Ni-Ti samples. The cells were allowed 24 h of contact with the samples, within this amount of time some cells spread to the bottom surface of both samples. With longer growth time, more cells could have been attached to the bottom surface. Normal cell attachment is important for successful integration of metal implants in the biological environment of the human body. Cells were formalin fixed to both Ni-Ti samples to observe cell morphology and cell attachment with SEM (Figure 11). After 24 h of adhesion, the morphology of fibroblasts is observed and is consistent with good adhesion and spreading. Cell adhesion and spreading indicate favorable biocompatibility of Ni-Ti, as previous studies have demonstrated [73,74].

These results support previous studies of *in vitro* biocompatibility of Ni-Ti [38,75–78]. Although Ni-Ti samples were sintered at different temperatures, results indicate that sintering temperature did not significantly affect cell viability. However, the average percentage area of cells attached to the Ni-Ti sample sintered at 1185 °C decreased in comparison to the sample sintered at 1175 °C. To determine if there were cells that did not attach to both Ni-Ti samples, the wells that the experiment was conducted in were evaluated. It was observed that there were no cells attached to the well plate, suggesting that the majority of cells attached to the sample. It is possible that more cells spread within the interconnected pore channels of the Ni-Ti sample sintered at 1185 °C than the sample sintered at 1175 °C, as previous studies have demonstrated [79,80]. Further investigation would need to be done to confirm that cells spread within the

interconnected pore channels of the Ni-Ti samples. The results of cell viability and cell attachment indicate favorable biocompatibility of Ni-Ti.

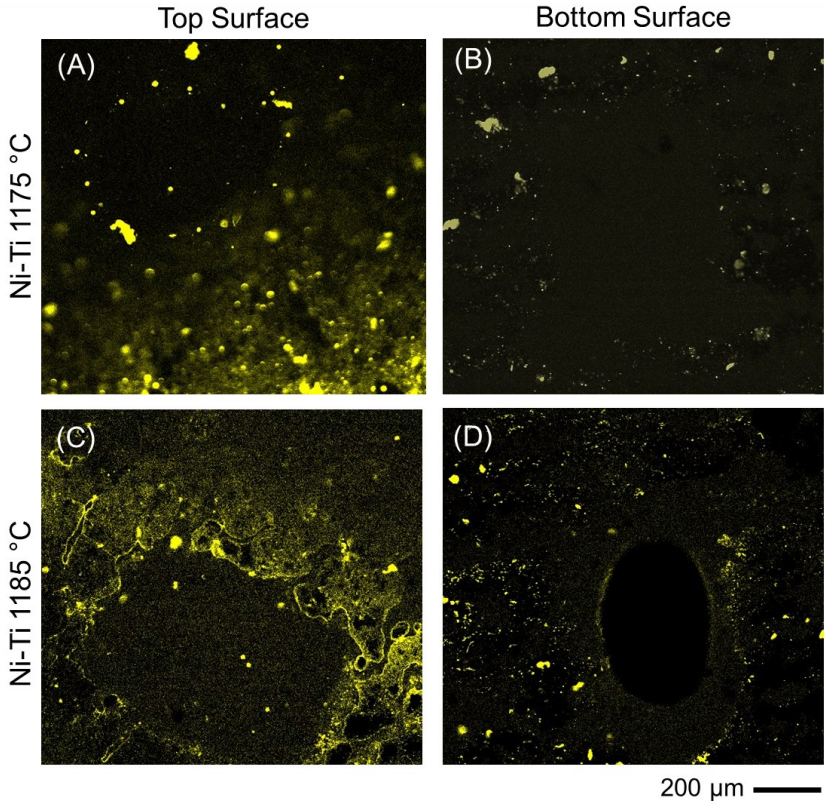

Figure 10. 3T3 fibroblasts attached to Ni-Ti 1175°C and Ni-Ti 1185°C. Fibroblasts were stained with PKH26 Red Fluorescent Cell membrane marker to observe cell attachment for 24 h on the Ni-Ti sample surfaces. Images were modified for stained cells to appear yellow. Cells spread through the interconnected pore channels and adhered to the top and bottom of both Ni-Ti surfaces (n = 2). (A) Cells attached to the top surface of Ni-Ti 1175°C with 11.6 ± 8.0% average percent area of cells attached. (B) Cells attached to the bottom surface of Ni-Ti 1175°C with 2.0 ± 1.0%. (C) Cells attached to the top surface of Ni-Ti 1185°C with 3.5 ± 3.0% average percent area of cells attached. (D) Cells attached to the bottom surface of Ni-Ti 1185°C with 1.1 ± 1.0%.

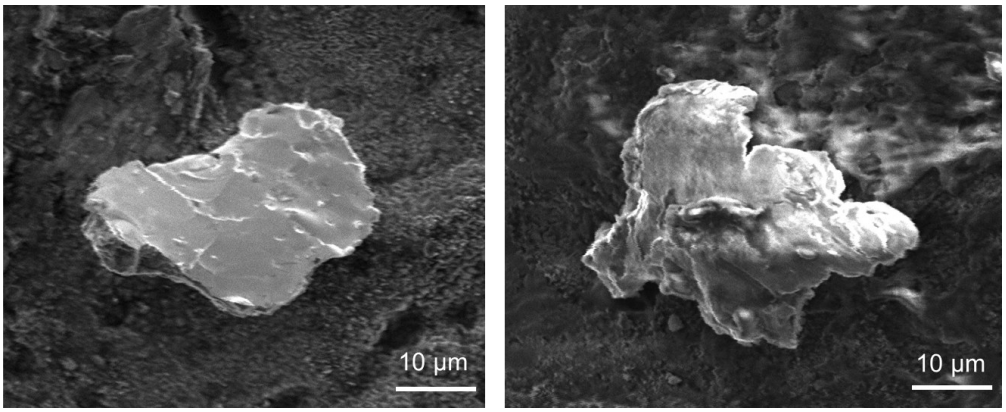

Figure 11. Exemplary SEM micrographs of 3T3 fibroblasts attached to Ni-Ti samples.

4. Conclusion

Ni-Ti powder was additively manufactured through binder jetting and solid-state sintering. The following remarks were made:

- The consolidated 3D-printed Ni-Ti parts demonstrate a clear relationship between pore morphology, pore fraction, and phase formation at varying sintering temperatures. Also, possible oxidation of Ni-Ti powder and formation of TiO_2 and $Ti_4Ni_2(O,C)$ was avoided by sintering in ultra-high purity Ar gas. At 1175 °C, the microstructure shows NiTi grains with TiC precipitates along grain boundaries and irregular, interconnected pores making up ~15% of the volume.

- Increase of the sintering temperature to 1185 °C results in the emergence of a minor Ni_3Ti and Ni_4Ti_3 and Ni_3Ti phases within NiTi grains, along with grain boundary TiC precipitates and isolated pores with a reduced volume fraction of around 5%. This higher sintering temperature correlates with an increased hardness (8.1±2.1 GPa compared to 6.9±1.2 GPa), reflecting a greater abundance of hard secondary phases and better densification.

- The DSC results do not detect transformation peaks for bulk-printed samples regardless of sintered condition; however, the structure with designed channels and thin struts provides transformation temperatures of A_s = -1 °C, A_f = 70 °C, M_s = 34 °C, and M_f = -36.5 °C. This observation suggests a geometry dependence of NiTi that calls for more studies. A shift to higher transformation temperatures is observed for the structure with designed channels and thin strut compared to the powder used in this study. This is well supported by the presence of Ni-rich secondary phases detected in the SEM study.

- The biocompatibility of Ni-Ti parts was assessed through tests of cell viability and attachment with 3T3 fibroblasts. Cell viability was evaluated by an indirect assessment of fibroblasts exposed to Ni-Ti leachates for 1 and 5 days. Results from day 1 and day 5 had high cell viability indicating favorable conditions for cell growth and survival. Cell attachment was a direct assessment of cell adherence to the surface of Ni-Ti. Results showed cell spreading and attachment on both Ni-Ti samples. These results suggest that binder jet sintered Ni-Ti has favorable biocompatibility as it does not significantly affect cell viability or adherence. Results from this experiment can be used to provide insight into

the use of binder jetted Ni-Ti for medical implants and tissue engineering applications. These results provide insight for future research to investigate different geometries and sintering conditions for NiTi structures that promote cell adherence and cell growth.

Acknowledgement

AM acknowledges the startup funding from the Department of Mechanical, Materials and Aerospace Engineering and Armour College of Engineering at Illinois Institute of Technology in Chicago, Illinois. AM gratefully acknowledges partial funding from the National Science Foundation [NSF grant number DMR-2050916 and CMMI-2339857]. The authors appreciate assistance from Nel Pretech Corporation (Mike Heim, Dave Nelson, and Antonio Gradi) with micro-computed tomography.

References

[1] L. Petrini, F. Migliavacca, Biomedical Applications of Shape Memory Alloys, J. Metall. 2011 (2011) 1–15.
[2] C. Greiner, S.M. Oppenheimer, D.C. Dunand, High strength, low stiffness, porous NiTi with superelastic properties, Acta Biomater. 1 (2005) 705–716.
[3] C.L. Chu, C.Y. Chung, P.H. Lin, S.D. Wang, Fabrication and properties of porous NiTi shape memory alloys for heavy load-bearing medical applications, J. Mater. Process. Technol. 169 (2005) 103–107.
[4] M.H. Elahinia, M. Hashemi, M. Tabesh, S.B. Bhaduri, Manufacturing and processing of NiTi implants: A review, Prog. Mater. Sci. 57 (2012) 911–946.
[5] S.E. Saghaian, M. Nematollahi, G.P. Toker, S.M.S. Narges Shayesteh Moghaddam, M. Radhakrishnan, O. Anderoglu, M. Elahinia, H. Karaca, Enhancing Shape Memory Response of Additively Manufactured Niti Shape Memory Alloys by Texturing and Post-Processing Heat Treatment, Shape Mem. Superelasticity. 9 (2023) 192–206.
[6] J. Khalil-Allafi, A. Dlouhy, G. Eggeler, Ni4Ti3-precipitation during aging of NiTi shape memory alloys and its influence on martensitic phase transformations, Acta Mater. 50 (2002) 4255–4274.
[7] Y. Liu, J. Van Humbeeck, R. Stalmans, L. Delaey, Some aspects of the properties of NiTi shape memory alloy, J. Alloys Compd. 247 (1997) 115–121.
[8] M. Bram, A. Ahmad-Khanlou, A. Heckmann, B. Fuchs, H.P. Buchkremer, D. Stöver, Powder metallurgical fabrication processes for NiTi shape memory alloy parts, Mater. Sci. Eng. A. 337 (2002) 254–263.
[9] K. Otsuka, X. Ren, Physical metallurgy of Ti-Ni-based shape memory alloys, Prog. Mater. Sci. 50 (2005) 511–678.
[10] O. Prymak, D. Bogdanski, M. Köller, S.A. Esenwein, G. Muhr, F. Beckmann, T. Donath, M. Assad, M. Epple, Morphological characterization and in vitro biocompatibility of a

porous nickel-titanium alloy, Biomaterials. 26 (2005) 5801–5807.
[11] Y. Yasenchuk, E. Marchenko, V. Gunther, A. Radkevich, O. Kokorev, S. Gunther, G. Baigonakova, V. Hodorenko, T. Chekalkin, J. hoon Kang, S. Weiss, A. Obrosov, Biocompatibility and clinical application of porous tini alloys made by self-propagating high-temperature synthesis (SHS), Materials (Basel). 12 (2019).
[12] J. Mentz, M. Bram, H.P. Buchkremer, D. Stöver, Improvement of mechanical properties of powder metallurgical NiTi shape memory alloys, Adv. Eng. Mater. 8 (2006) 247–252.
[13] R. Purohit, K.K. Patel, G.K. Gupta, R.S. Rana, Development of Ni-Ti Shape Memory Alloys through Novel Powder Metallurgy Route and Effect of Rolling on their properties, Mater. Today Proc. 4 (2017) 5330–5335.
[14] S. Parvizi, S.M. Hashemi, F. Asgarinia, M. Nematollahi, M. Elahinia, Effective parameters on the final properties of NiTi-based alloys manufactured by powder metallurgy methods: A review, Prog. Mater. Sci. 117 (2021) 100739.
[15] S. Parvizi, V. Hasannaeimi, E. Saebnoori, T. Shahrabi, S.K. Sadrnezhaad, Fabrication of porous NiTi alloy via powder metallurgy and its mechanical characterization by shear punch method, Russ. J. Non-Ferrous Met. 53 (2012) 169–175.
[16] M.H. Ismail, R. Goodall, H.A. Davies, I. Todd, Formation of microporous NiTi by transient liquid phase sintering of elemental powders, Mater. Sci. Eng. C. 32 (2012) 1480–1485.
[17] S. Saedi, S.E. Saghaian, A. Jahadakbar, N. Shayesteh Moghaddam, M. Taheri Andani, S.M. Saghaian, Y.C. Lu, M. Elahinia, H.E. Karaca, Shape memory response of porous NiTi shape memory alloys fabricated by selective laser melting, J. Mater. Sci. Mater. Med. 29 (2018).
[18] B. Yuan, C.Y. Chung, M. Zhu, Microstructure and martensitic transformation behavior of porous NiTi shape memory alloy prepared by hot isostatic pressing processing, Mater. Sci. Eng. A. 382 (2004) 181–187.
[19] E. Schüller, M. Bram, H.P. Buchkremer, D. Stöver, Phase transformation temperatures for NiTi alloys prepared by powder metallurgical processes, Mater. Sci. Eng. A. 378 (2004) 165–169.
[20] S.M. Green, D.M. Grant, N.R. Kelly, Powder metallurgical processing of Ni-Ti shape memory alloy, Powder Metall. 40 (1997) 43–47.
[21] C.L. Chu, C.Y. Chung, P.H. Lin, S.D. Wang, Fabrication of porous NiTi shape memory alloy for hard tissue implants by combustion synthesis, Mater. Sci. Eng. A. 366 (2004) 114–119.
[22] S.K. Sadrnezhaad, S.A. Hosseini, Fabrication of porous NiTi-shape memory alloy objects by partially hydrided titanium powder for biomedical applications, Mater. Des. 30 (2009) 4483–4487.
[23] N.M. Dawood, A.R.K. Abid Ali, A.A. Atiyah, Fabrication of Porous NiTi Shape Memory Alloy Objects by Powder Metallurgy for Biomedical Applications, IOP Conf. Ser. Mater. Sci. Eng. 518 (2019).
[24] M. Daly, A. Pequegnat, Y. Zhou, M.I. Khan, Enhanced thermomechanical functionality of a laser processed hybrid NiTiNiTiCu shape memory alloy, Smart Mater. Struct. 21 (2012).
[25] M. Daly, A. Pequegnat, Y.N. Zhou, M.I. Khan, Fabrication of a novel laser-processed NiTi shape memory microgripper with enhanced thermomechanical functionality, J. Intell. Mater. Syst. Struct. 24 (2013) 984–990.
[26] A. Mostafaei, C. Zhao, Y. He, S. Reza Ghiaasiaan, B. Shi, S. Shao, N. Shamsaei, Z. Wu,

N. Kouraytem, T. Sun, J. Pauza, J. V. Gordon, B. Webler, N.D. Parab, M. Asherloo, Q. Guo, L. Chen, A.D. Rollett, Defects and anomalies in powder bed fusion metal additive manufacturing, Curr. Opin. Solid State Mater. Sci. 26 (2022) 100974.
[27] M. Elahinia, N. Shayesteh Moghaddam, M. Taheri Andani, A. Amerinatanzi, B.A. Bimber, R.F. Hamilton, Fabrication of NiTi through additive manufacturing: A review, Prog. Mater. Sci. 83 (2016) 630–663.
[28] A. Mostafaei, A.M. Elliott, J.E. Barnes, F. Li, W. Tan, C.L. Cramer, P. Nandwana, M. Chmielus, Binder jet 3D printing—Process parameters, materials, properties, modeling, and challenges, Prog. Mater. Sci. 119 (2021) 100707.
[29] M. Mariani, N. Lecis, A. Mostafaei, Binder Jetting-based Metal Printing, in: Solid-State Met. Addit. Manuf. Physics, Process. Mech. Prop. Appl., John Wiley & Sons, 2024: pp. 339–357.
[30] J.W. Sears, C. Allen, A. Holliday, Binder-Jet 3D Direct Metal Printing of Cobalt Chrome Moly Alloy, AMPM 2019 Conf. Phoenix, Arizona. (2019).
[31] E. Wheat, M. Vlasea, J. Hinebaugh, C. Metcalfe, Sinter structure analysis of titanium structures fabricated via binder jetting additive manufacturing, Mater. Des. 156 (2018) 167–183.
[32] E. Sheydaeian, E. Toyserkani, Additive manufacturing functionally graded titanium structures with selective closed cell layout and controlled morphology, Int. J. Adv. Manuf. Technol. 96 (2018) 3459–3469.
[33] E. Wheat, Process Mapping and Optimization of Titanium Parts Made by Binder Jetting Additive Manufacturing by, (2018).
[34] A. Mostafaei, P.R. De Vecchis, M.J. Buckenmeyer, S.R. Wasule, B.N. Brown, M. Chmielus, Microstructural evolution and resulting properties of differently sintered and heat-treated binder jet 3D printed Stellite 6, Mater. Sci. Eng. C. 102 (2019) 276–288.
[35] M. Khademitab, P. Rodriguez, D. Vecchis, P. Staszel, M.K. Vaicik, M. Chmielus, A. Mostafaei, Structure-property relationships of differently heat-treated binder jet printed Co-Cr-Mo biomaterial, Mater. Today Commun. 38 (2024) 107716.
[36] B.J. Paudel, A.C. To, A. Mostafaei, Principles of Solid-State Sintering, in: Solid-State Met. Addit. Manuf. Physics, Process. Mech. Prop. Appl., John Wiley & Sons, 2024: pp. 297–312.
[37] D. Zhang, Y. Li, H. Wang, W. Cong, An investigation on Ni4Ti3 phase precipitation and its effects in laser directed energy deposition of TiC–NiTi composites, Mater. Sci. Eng. A. 809 (2021) 140976.
[38] O. V Kokorev, V.N. Khodorenko, S.G. Anikeev, V.E. Gunther, BIOTECHNOLOGIES Biocompatibility of Textile Titanium Nickel Implants with Fibroblast Culture, 159 (2015) 87–91.
[39] S. Knoedler, S. Broichhausen, R. Guo, R. Dai, L. Knoedler, M. Kauke-Navarro, F. Diatta, B. Pomahac, H.G. Machens, D. Jiang, Y. Rinkevich, Fibroblasts – the cellular choreographers of wound healing, Front. Immunol. 14 (2023) 1–16.
[40] A. Mostafaei, P. Rodriguez De Vecchis, E.L.E.L. Stevens, M. Chmielus, Sintering regimes and resulting microstructure and properties of binder jet 3D printed Ni-Mn-Ga magnetic shape memory alloys, Acta Mater. 154 (2018) 355–364.
[41] A. Mostafaei, K.A. Kimes, E.L. Stevens, J. Toman, Y.L. Krimer, K. Ullakko, M. Chmielus, Microstructural evolution and magnetic properties of binder jet additive manufactured Ni-Mn-Ga magnetic shape memory alloy foam, Acta Mater. 131 (2017)

482–490.
[42] M. Jamalkhani, M. Asherloo, O. Gurlekce, I.-T. Ho, M. Heim, D. Nelson, A. Mostafaei, Deciphering microstructure-defect-property relationships of vacuum-sintered binder jetted fine 316L austenitic stainless steel powder, Addit. Manuf. 59 (2022) 103133.
[43] W.C. Oliver, G.M. Pharr, Measurement of hardness and elastic modulus by instrumented indentation: Advances in understanding and refinements to methodology, J. Mater. Res. 19 (2004) 3–20.
[44] ISO 10993-5:2009, Biological evaluation of medical devices, Part 5: Tests for in vitro cytotoxicity, 2009.
[45] C. Zheng, A. Mostafaei, P.R. de Vecchis, I. Nettleship, M. Chmielus, Microstructure evolution for isothermal sintering of binder jet 3D printed alloy 625 above and below the solidus temperature, Addit. Manuf. 47 (2021) 102276.
[46] A. Mostafaei, P. Rodriguez De Vecchis, I. Nettleship, M. Chmielus, Effect of powder size distribution on densification and microstructural evolution of binder-jet 3D-printed alloy 625, Mater. Des. 162 (2019) 375–383.
[47] N.D. Parab, J.E. Barnes, C. Zhao, R.W. Cunningham, A.D. Rollett, T. Sun, Real time observation of binder jetting printing process using high-speed X-ray imaging, Sci. Rep. (2019) 28–30.
[48] M. Jamalkhani, M. Dorula, E. Roberts, A. Mostafaei, Densification kinetics, microstructural evolution and mechanical properties of isothermally sintered binder jetted 316L stainless steel, J. Manuf. Process. 125 (2024) 267–282.
[49] P. Rodriguez De Vecchis, A. Mostafaei, M. Chmielus, Densification kinetics and microstructural evolution of binder jet printed and sintered porous Ni-Mn-Ga magnetic shape-memory alloys, Acta Mater. 260 (2023) 119323.
[50] S.K. Patel, A. Behera, Evolution of Phases and their Influence on Shape Memory Effect by Varying Sintering Parameters of NiTi Alloys, Met. Mater. Int. 28 (2022) 2691–2705.
[51] A. Babaei-dehkordi, M. Soltanieh, M. Mirjalili, M. Asherloo, Understanding Interfacial Reactions in Ti – Ni Diffusion Couple, Materials (Basel). 16 (2023) 2267.
[52] W. Prendota, K. Goc, T. Strączek, E. Yamada, A. Takasaki, J. Przewoźnik, A. Radziszewska, S. Uematsu, C. Kapusta, Properties of niti shape memory alloy micro-foils obtained by pulsed-current sintering of ni/ti foils, Metals (Basel). 9 (2019).
[53] A.S. Jabur, J.T. Al-Haidary, E.S. Al-Hasani, Characterization of Ni-Ti shape memory alloys prepared by powder metallurgy, J. Alloys Compd. 578 (2013) 136–142.
[54] a. a. Antonysamy, J. Meyer, P.B. Prangnell, Effect of build geometry on the β-grain structure and texture in additive manufacture of Ti6Al4V by selective electron beam melting, Mater. Charact. 84 (2013) 153–168.
[55] J. Frenzel, Z. Zhang, C. Somsen, K. Neuking, G. Eggeler, Influence of carbon on martensitic phase transformations in NiTi shape memory alloys, Acta Mater. 55 (2007) 1331–1341.
[56] S. Ehsan Saghaian, M. Nematollahi, G. Toker, A. Hinojos, N. Shayesteh Moghaddam, S. Saedi, C.Y. Lu, M. Javad Mahtabi, M.J. Mills, M. Elahinia, H.E. Karaca, Effect of hatch spacing and laser power on microstructure, texture, and thermomechanical properties of laser powder bed fusion (L-PBF) additively manufactured NiTi, 2022.
[57] W.D. Kingery, M.D. Narasimhan, Densification during Sintering in the Presence of a Liquid Phase. II. Experimental, J. Appl. Phys. 30 (1959) 307–310.
[58] G.. Kuczynski, The mechanism of densification during sintering of metallic particles, Acta

Metall. 4 (1956) 58–61.
[59] R. Arifin, M. Malyadi, Munaji, G.A. Buntoro, Darminto, Evaluation of melting behaviour of Nickel, Titanium, and NiTi alloy using EAM and MEAM type potential, J. Phys. Conf. Ser. 1171 (2019).
[60] P. Nandwana, R. Kannan, D. Siddel, Microstructure evolution during binder jet additive manufacturing of H13 tool steel, Addit. Manuf. 36 (2020) 101534.
[61] M. Khademitab, M. Jamalkhani, K. Bishaj, E. Jenssen, M. Heim, D. Nelson, N.M. O'Dowd, A. Mostafaei, Does Selective Shell Printing Advance Binder Jetting Additive Manufacturing?, Powder Technol. 441 (2024) 119812.
[62] A. Cabo Rios, T. Mishurova, L. Cordova, M. Persson, G. Bruno, E. Olevsky, E. Hryha, Ex-situ characterization and simulation of density fluctuations evolution during sintering of binder jetted 316L, Mater. Des. 238 (2024) 112690.
[63] E. Stevens, K. Kimes, D. Salazar, A. Mostafaei, R. Rodriguez, A. Acierno, P. Lázpita, V. Chernenko, M. Chmielus, Mastering a 1.2 K hysteresis for martensitic para-ferromagnetic partial transformation in Ni-Mn(Cu)-Ga magnetocaloric material via binder jet 3D printing, Addit. Manuf. (2020).
[64] K.M. Rahman, A. Wei, H. Miyanaji, C.B. Williams, Impact of Binder on Part Densification: Enhancing Binder Jetting Part Properties through the Fabrication of Shelled Geometries, Sensors Actuators B. Chem. 62 (2023) 103377.
[65] A. Mostafaei, P.R. De Vecchis, K.A. Kimes, D. Elhassid, M. Chmielus, Effect of binder saturation and drying time on microstructure and resulting properties of sinter-HIP binder-jet 3D-printed WC-Co composites, Addit. Manuf. 46 (2021) 102128.
[66] R.K. Enneti, K.C. Prough, Effect of binder saturation and powder layer thickness on the green strength of the binder jet 3D printing (BJ3DP) WC-12%Co powders, Int. J. Refract. Met. Hard Mater. (2019) 104991.
[67] D. Gilmer, S. Kim, D.J. Goldsby, P. Nandwana, A. Elliott, T. Saito, Predictive binder jet additive manufacturing enabled by clean burn-off binder design, Addit. Manuf. 80 (2024) 103955.
[68] M.M. Islam, P. Bayati, M. Nematollahi, A. Jahadakbar, M. Elahinia, M. Haghshenas, Ambient-temperature indentation creep of shape memory niti alloys: Additively manufactured versus cast, J. Manuf. Mater. Process. 5 (2021).
[69] S. Saedi, A.S. Turabi, M.T. Andani, C. Haberland, H. Karaca, M. Elahinia, The influence of heat treatment on the thermomechanical response of Ni-rich NiTi alloys manufactured by selective laser melting, J. Alloys Compd. 677 (2016) 204–210.
[70] M. Arciniegas, J. Casals, J.M. Manero, J. Peña, F.J. Gil, Study of hardness and wear behaviour of NiTi shape memory alloys, J. Alloys Compd. 460 (2008) 213–219.
[71] M. Farvizi, T. Ebadzadeh, M.R. Vaezi, E.Y. Yoon, Y.J. Kim, J.Y. Kang, H.S. Kim, A. Simchi, Effect of starting materials on the wear performance of NiTi-based composites, Wear. 334–335 (2015) 35–43.
[72] M.R. Akbarpour, S. Alipour, M. Najafi, T. Ebadzadeh, H.S. Kim, Microstructural characterization and enhanced hardness of nanostructured Ni3Ti– NiTi (B2) intermetallic alloy produced by mechanical alloying and fast microwave-assisted sintering process, Intermetallics. 131 (2021) 107119.
[73] C. Wirth, V. Comte, C. Lagneau, P. Exbrayat, M. Lissac, N. Jaffrezic-Renault, L. Ponsonnet, Nitinol surface roughness modulates in vitro cell response: A comparison between fibroblasts and osteoblasts, Mater. Sci. Eng. C. 25 (2005) 51–60.

[74] L. Ponsonnet, V. Comte, A. Othmane, C. Lagneau, M. Charbonnier, M. Lissac, N. Jaffrezic, Effect of surface topography and chemistry on adhesion, orientation and growth of fibroblasts on nickel-titanium substrates, Mater. Sci. Eng. C. 21 (2002) 157–165.
[75] O. Prymak, D. Bogdanski, M. Ko, S.A. Esenwein, G. Muhr, F. Beckmann, T. Donath, M. Assad, M. Epple, Morphological characterization and in vitro biocompatibility of a porous nickel – titanium alloy, 26 (2005) 5801–5807.
[76] S. Rhalmi, M. Odin, M. Assad, M. Tabrizian, C.H. Rivard, L.H. Yahia, Hard, soft tissue and in vitro cell response to porous nickel-titanium: A biocompatibility evaluation, Biomed. Mater. Eng. 9 (1999) 151–162.
[77] T.T. Nguyen, C.C. Hu, B.Y. Chou, C.Y. Chou, G.Y. Lin, Y.C. Hu, Y.L. Chen, W.T. Hsu, Z.S. Lin, Y.L. Lee, C.H. Chen, H.W. Yen, R.J. Chung, Evaluating hydrogenated nickel-titanium alloy for orthopedic implant, J. Mater. Res. Technol. 18 (2022) 1115–1123.
[78] M. Assad, N. Lemieux, C.H. Rivard, Assad et al. - 1999 - Bio-medical materials and engineering, 9 (1999) 1–12.
[79] S. Van Bael, Y.C. Chai, S. Truscello, M. Moesen, G. Kerckhofs, H. Van Oosterwyck, J.P. Kruth, J. Schrooten, The effect of pore geometry on the in vitro biological behavior of human periosteum-derived cells seeded on selective laser-melted Ti6Al4V bone scaffolds, Acta Biomater. 8 (2012) 2824–2834.
[80] K.C. Nune, A. Kumar, R.D.K. Misra, S.J. Li, Y.L. Hao, R. Yang, Osteoblast functions in functionally graded Ti-6Al-4 v mesh structures, J. Biomater. Appl. 30 (2016) 1182–1204.